



The effect of yield stress on pipe flow turbulence for generalised newtonian fluids



J. Singh*, M. Rudman, H.M. Blackburn

Department of Mechanical and Aerospace Engineering, Monash University, VIC 3800, Australia

ARTICLE INFO

Keywords:

Turbulent pipe flow
Direct numerical simulations (DNS)
Yield stress

ABSTRACT

The effect of modifying yield stress on turbulent pipe flow of generalised Newtonian fluids at a friction Reynolds number of 323 is investigated using direct numerical simulations. Simulations are carried out for Bingham and Herschel–Bulkley fluids with the yield stress varying from 0% to 20% of the mean wall shear stress. Results show that the effect of increasing yield stress is mostly similar to shear thinning in power-law fluids. The turbulent viscous stress which arises due to viscosity fluctuations is negative for a yield stress fluid and is higher in magnitude for higher yield stress. An analysis of the turbulent kinetic energy budget showed that the effect of yield stress is mainly significant near the wall for $y^+ \lesssim 60$ which was also seen for shear-thinning power-law fluids at similar Re_τ . Additional shear thinning enhances the yield stress effect. The main difference between shear thinning and yield stress is that the effect of yield stress is maximum outside the viscous sublayer whereas shear thinning has a more significant effect inside the viscous sublayer.

1. Introduction

Many fluids found in industry and in nature do not show a uniform viscosity. These fluids are called non-Newtonian fluids. Generalised Newtonian fluids is a class of non-Newtonian fluids for which the rheology can be modelled via the generalised Newtonian (GN) assumption

$$\tau = \rho\nu(\dot{\gamma})\mathbf{s}. \quad (1)$$

Here τ is the shear stress tensor, ρ is fluid density, ν is fluid kinematic viscosity (also called the effective viscosity), shear rate $\dot{\gamma} = (2\mathbf{s} : \mathbf{s})^{1/2}$ is the second invariant of the strain rate tensor $\mathbf{s} = [(\nabla\mathbf{v}) + (\nabla\mathbf{v})^T]/2$ and \mathbf{v} is the velocity. The GN assumption also implies an isotropic, time-independent viscosity and an instantaneous response of the fluid to the applied shear stress. Many GN fluids show yield stress i.e. they do not flow until the shear stress exceeds a minimum value (yield stress). Mining slurries, particle suspensions, waste water sludge, toothpaste, cements, tomato ketchup, melted chocolate are examples of yield stress GN fluids. Recently the Journal of non-Newtonian fluid mechanics published a special issue (the first special virtual issue, 2014) focusing only on yield stress fluids, which shows the continuing research interest in these fluids.

The effective viscosity of a GN fluid is defined via a rheology model. There are various rheology models available for yield stress GN fluids [1,2] in which the Herschel–Bulkley rheology model is a widely used

model which relates the fluid kinematic viscosity to the shear rate via

$$\nu = \rho^{-1}(\tau_y/\dot{\gamma} + K\dot{\gamma}^{n-1}). \quad (2)$$

Here, the yield stress τ_y , fluid consistency K and the flow index n are model parameters. For $n < 1$, Eq. (2) represents shear-thinning behaviour i.e. the fluid viscosity decreases with increasing shear rate. With $n = 1.0$, Eq. (2) reduces to the Bingham rheology model $\nu = \rho^{-1}(\tau_y/\dot{\gamma} + K)$, with K known as plastic viscosity. When $\tau_y = 0$, Eq. (2) reduces to a power-law rheology model which represents purely shear-thinning (or thickening) behaviour. It is worth noting that rheology model parameters are usually determined via regression using an experimentally measured shear rheogram (one dimensional shear stress versus shear rate measurements) and have no intrinsic physical meaning. In the following Herschel–Bulkley (HB), Bingham and power-law (PL) fluids are those whose rheology can be well-modelled with the corresponding model.

Turbulent pipe flow is an important class of wall bounded turbulent flows. A pipe flow has the characteristic feature of an enclosed geometry, making it easiest to realise in experiments compared to other wall bounded flows such as channel and boundary layer flows [3]. It also has a direct and familiar application – pipeline transport which is very common at mining and waste water treatment sites to transport slurries which can show both yield stress and shear-thinning behaviour and the rheology of which can be modelled via the HB rheology model [4]. In spite of wide applications, studies of turbulent pipe flow of HB

* Corresponding author.

E-mail address: jagmohan.singh@monash.edu (J. Singh).

fluids are limited [5–9].

The HB rheology combines the effect of yield stress and shear thinning (or thickening). It has been shown that the HB rheology delays transition to turbulence to a higher Reynolds number and reduces the turbulent friction factor $f = 2\tau_w/\rho U_b^2$ under fully developed turbulent conditions [5,7,8]. The HB rheology increases the turbulent anisotropy by increasing the velocity fluctuations in the axial direction but decreasing the same in the radial and the azimuthal direction compared to Newtonian fluid. These trends are consistent with those of a shear-thinning fluid alone [7], therefore, the effect of the yield stress alone on turbulent pipe flow dynamics is not clear. Peinixinho et al. [10] claimed that the yield stress did not have a significant effect in the turbulent regime, however, fluids used in that study showed some viscoelastic behaviour, and the effect of yield stress is less clear.

In real fluids the rheology model parameters are generally coupled with each other. The rheology arises from surface effects in fine particle suspensions and polymer interaction in polymer based lab fluids. The rheology is changed by modifying concentration and potentially pH, however, such changes generally modify all rheology parameters [11–13], and it is difficult to change just one while keeping others constant. This makes experimental investigation of individually varying rheology model parameters impossible. Numerical simulations, especially direct numerical simulations (DNS) are promising in this aspect and have been used in the past in turbulent flow studies of HB fluids [7,8]. Although significant discrepancies had been observed between numerical and experimental results [8], recently these have been shown to be caused by a lack of high shear rate data used in rheology characterisation [14]. DNS provides a detailed picture of the flow and once validated, can be reliably used to understand the effect of individually varying rheology model parameters. DNS has other advantage that unlike other numerical techniques such as Reynolds averaged Navier–Stokes (RANS) and large eddy simulations (LES), it does not require any special model to capture the flow at small length scales. There have been some efforts in developing RANS and LES models for GN fluids [9,15–17] but there are no universally accepted models yet available.

Turbulent flows present a wide range of length scales (eddy sizes) and the HB rheology decreases the range of the length scales in the flow [7]. Earlier DNS studies of HB fluids [7,8] considered flow indices $n = 0.52$ and 0.6 with a maximum Reynolds number Re_G (defined in Section 2.2) of 8000. However, the flows showed some transitional behaviour especially for $n = 0.52$. To overcome this limitation, the current study considers a slightly higher Reynolds number $Re_G \approx 11000$ ($Re_\tau = 323$) to study the effect of yield stress τ_y on a turbulent pipe flow. To study the effect of varying τ_y alone, simulations are run using the Bingham rheology model with the yield stress varying from 0% to 20% of the mean wall shear stress. Additional simulations with the HB rheology model are run to study the effect of additional shear thinning. The results of mean flow, turbulence intensities and the turbulent kinetic energy budget are analysed and compared with those of Newtonian and PL fluids. The key findings are that the effect of yield stress is confined to the near wall region and unlike shear thinning it affects flow most noticeably outside the viscous sublayer.

2. Methodology

2.1. Numerical method

The numerical method used here is identical to that used in Rudman & Blackburn [7,8,18]. Here we briefly review the simulation methodology. A nodal spectral element-Fourier DNS code is used to solve the governing equations (Eq. 3) for an incompressible fluid with a spatially varying viscosity.

$$D\mathbf{v}/Dt = \rho^{-1}(-\nabla p + \nabla \cdot \boldsymbol{\tau} + \rho \mathbf{g}), \quad \text{with} \quad \nabla \cdot \mathbf{v} = 0 \quad (3)$$

where \mathbf{v} is the velocity vector, p is the static pressure, $\boldsymbol{\tau}$ is the stress

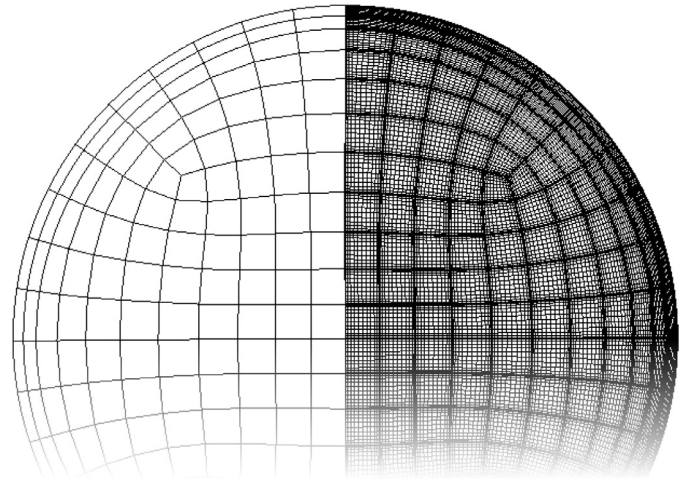


Fig. 1. Detail of a spectral-element mesh used to discretise pipe cross-section, illustrating grid nodes for 12th-order element interpolation functions, $N_p = 12$.

tensor and $\rho \mathbf{g}$ is the body force. For ease of notation, we divide p , $\boldsymbol{\tau}$ and $\rho \mathbf{g}$ in Eq. (3) by the constant fluid density ρ , but refer to them as pressure, stress and body force respectively. The body force \mathbf{g} is set equal to the mean axial pressure gradient. The modified shear stress tensor, $\boldsymbol{\tau}/\rho$, is modelled via the GN assumption (Eq. 1) and the fluid viscosity, $\nu(\dot{\gamma})$, is modelled via the HB rheology model. The governing equations are solved in Cartesian coordinates where the pipe cross section (x - y plane) is discretized using spectral elements as shown in Fig. 1, while Fourier expansion is used in the axial (z) direction. Results are later transformed for presentation in cylindrical coordinates. The code has been validated for DNS of pipe flow of turbulent Newtonian fluids [18] and non-Newtonian fluids [8,14]. For more details of the simulations code we refer the reader to [7,8,19].

2.2. Reynolds number

The non-uniform viscosity of GN fluids makes the choice of an appropriate viscosity scale unclear. We choose the nominal wall viscosity, ν_w , for the viscosity scale as discussed by Rudman et al. [7]. For the HB rheology model, ν_w is given as:

$$\nu_w = \frac{1}{\rho} \frac{K^{1/n} \tau_w}{(\tau_w - \tau_y)^{1/n}}. \quad (4)$$

Here τ_w is the mean wall shear stress which is determined from the mean axial pressure gradient $\partial P/\partial z$ as:

$$\tau_w = (R/2)(\partial P/\partial z) \quad (5)$$

where R is the pipe radius. Using ν_w , pipe diameter $D = 2R$, bulk flow velocity U_b (flow rate per unit area) and the friction velocity $u^* = (\tau_w/\rho)^{1/2}$, we define the generalised Reynolds number Re_G and the friction Reynolds number Re_τ as:

$$Re_G = U_b D/\nu_w \quad \text{and} \quad Re_\tau = u^* R/\nu_w. \quad (6)$$

2.3. Simulation parameters and non-dimensional variables

Simulations are run for a fixed friction Reynolds number Re_τ of 323 which is equivalent to a generalised Reynolds number $Re_G \approx 11,000$ (Re_G slightly varies with n and τ_y , see Table 1). The effect of τ_y alone is studied with $n = 1.0$ (Bingham rheology model) and τ_y varying from 0% (Newtonian) to 20% of τ_w . Additional simulations with $n = 0.8$ and $\tau_y = 0\%$ (PL) and 10% of τ_w are carried out to study the additional effect of shear thinning.

Results are normalised using the friction velocity $u^* = (\tau_w/\rho)^{1/2}$ for the velocity scale and ν_w/u^* for the length scale. Hence the distance

Table 1
Simulation parameters for pipe flow of different n and τ_y at $Re_\tau = 323$. Non-dimensional body force gR/u^{*2} is fixed at 2 and the nominal wall viscosity $\nu_w/(u^*R)$ is fixed at $1/323$.

Identifier	n	$K/(\rho u^{*2-n} R^n)$	$\tau_y^+ = \tau_y/\tau_w(\%)$	U_b/u^*	Re_G
Newt.	1.0	3.0870×10^{-3}	0	15.93	10,322
Bi5	1.0	2.9399×10^{-3}	5	16.12	10,463
Bi10	1.0	1.3927×10^{-3}	10	16.49	10,635
Bi20	1.0	1.2379×10^{-3}	20	17.23	11,103
PL	0.8	9.8128×10^{-3}	0	16.49	10,681
HB10	0.8	2.8352×10^{-3}	10	17.05	11,036

from the wall is expressed in wall coordinates as $y^+ = (R - r)u^*/\nu_w$, where r is the radial distance from the pipe centre. The non-dimensional turbulence intensities are expressed as $u_i^{*+} = (\overline{u_i'^2})^{1/2}/u^*$. Shear stress is normalised by τ_w , shear rate by u^{*2}/ν_w and the turbulent kinetic energy budget terms by u^{*4}/ν_w . In the current simulations, τ_w (and hence the axial body force) and ν_w are fixed for all cases and the consistency is calculated using Eq. (4) for a given τ_y . The simulation parameters are given in Table 1. Non-dimensional body force gR/u^{*2} is fixed at 2 and the nominal wall viscosity $\nu_w/(u^*R)$ is fixed at $1/323$ in all simulations. The consistency K decreases with increasing τ_y to maintain constant Re_τ . Increasing τ_y increases the bulk velocity U_b , which increases further as the fluid becomes more shear-thinning (HB10 has higher U_b than Bi10). The fluid viscosity is plotted as a function of shear rate in Fig. 2. As set the fluid viscosity is the same at the wall shear rate $\dot{\gamma} = \gamma_w$ ($\dot{\gamma}^+ = 1$ in Fig. 2) in all simulations. Fluid viscosity increases for $\dot{\gamma} < \gamma_w$ ($\dot{\gamma}^+ < 1$) with increasing τ_y or shear thinning but decreases for $\dot{\gamma} > \gamma_w$ ($\dot{\gamma}^+ > 1$).

2.4. Details of mesh, domain and time averaging

A mesh and domain independence study was carried out in [18] for a Newtonian fluid at the same Re_τ to ensure that the second and higher order turbulence statistics do not vary with further mesh refinement or with increasing the domain length. The same mesh and the domain length is used here for all simulations. Since turbulent eddies are expected to grow in size with increasing τ_y or shear thinning, this means that the mesh will not be under-resolved. The two points correlations of the axial velocity fluctuations (shown later for Bingham fluids in Fig. 4 for two different y^+) decay to zero, which shows adequacy of the domain length. The mesh had 300 spectral elements of polynomial order 12 and 384 axial planes (192 Fourier modes) and the domain is approximately $12D$ long. This gives a near wall mesh spacing of $\Delta y^+ = 0.8$ in the wall normal direction, $\Delta r\theta^+ \approx 4.5$ in the azimuthal direction and $\Delta z^+ \approx 21$ in the axial direction.

Simulations are run until the calculated instantaneous wall shear stress and bulk velocity had reached a statistically steady state value before collecting averages. The time-averaged statistics are then collected for approximately 15 transit times of the domain.

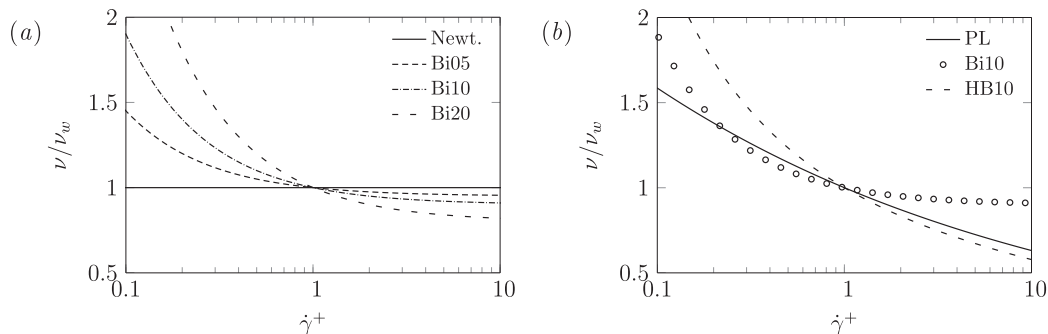


Fig. 2. Viscosity rheograms plotted for (a) Newtonian and Bingham fluids (b) power-law, Herschel-Bulkley and Bi10 fluids from Table 1. The effect of the yield stress is seen mainly at shear rates lower than $\dot{\gamma}_w^+$.

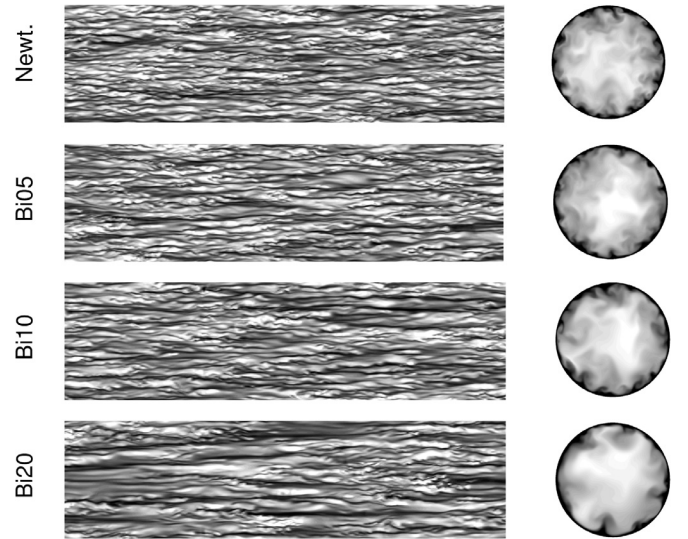


Fig. 3. Instantaneous axial velocity contours (left) at $y^+ = 10$ shown on developed cylindrical surfaces and (right) at a cross section plotted for (from top) Newtonian fluid and Bingham fluids Bi5, Bi10 and Bi20. Flow is from left to right, and lighter grey represents higher speed. Flow becomes more transitional as the yield stress is increased.

3. Results and discussions

3.1. The effect of yield stress

We first present the results from Bingham fluids and compare them with the Newtonian. Wherever appropriate the yield stress effect here is compared with that of shear thinning alone (i.e. PL rheology with $n < 1$) as presented in [18].

Fig. 3 shows contours of instantaneous axial velocity near the wall (in the buffer layer at $y^+ = 10$) and at a cross section. Despite having the same nominal wall viscosity ν_w , differences in the flow of these fluids are clear. Increasing τ_y reduces the fluctuations in the flow and low speed streaks run longer in the streamwise direction for a higher τ_y . This is similar to the effect of pure shear thinning [18].

The information illustrated in Fig. 3 can be quantified using the integral length scale which is calculated by integrating the two point correlation function to a point where it first crosses zero (for more details see [18]). For streamwise velocity fluctuations, the two point correlation is defined as:

$$\rho_{u'_z u'_z}(\Delta z) = \langle u'_z(r, \theta, z, t) u'_z(r, \theta, z + \Delta z, t) \rangle / \langle u'_z(r, \theta, z)^2 \rangle$$

$$\rho_{u'_z u'_z}(\Delta \theta) = \langle u'_z(r, \theta, z, t) u'_z(r, \theta + \Delta \theta, z, t) \rangle / \langle u'_z(r, \theta, z)^2 \rangle. \quad (7)$$

Profiles of the two point correlation of the axial velocity fluctuations $\rho_{u'_z u'_z}$ are plotted as a function of the axial separation distance $\Delta z/D$ in Fig. 4. The two point correlation function $\rho_{u'_z u'_z}$ decays to zero which as

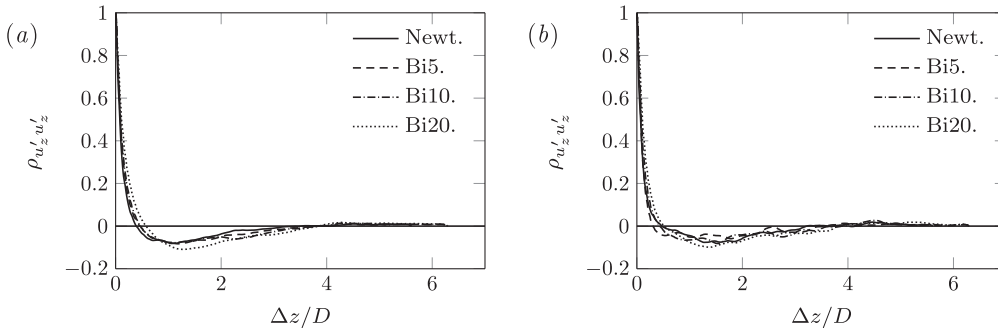


Fig. 4. Two point correlation plot for the streamwise velocity fluctuations ($\rho u'_z u'_z$) plotted as a function of the separation distance $\Delta z/D$ at (a) $y^+ = 10$ and (b) $y^+ = 100$.

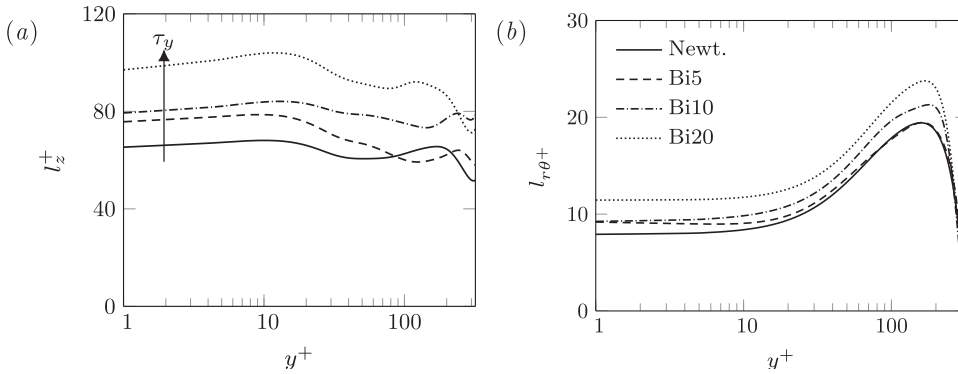


Fig. 5. Profiles of the (a) streamwise integral length scale and (b) azimuthal integral length scale plotted as a function of y^+ for different τ_y .

mentioned in Section 2 shows the adequacy of the domain length. Profiles of streamwise and azimuthal integral length scales (in wall units l_z^+ and $l_{r\theta}^+$) of axial velocity fluctuations (Fig. 5 a, and b) shows that the integral length scale of the axial velocity fluctuations in both streamwise and azimuthal directions near the wall increases with τ_y . This is similar to the effect of shear thinning in PL fluids (Fig. 7 in [18]). However, unlike PL fluids, here the profiles of the streamwise integral length scale l_z^+ cross each other away from the wall for Bi5 and Newtonian (Fig. 5 a). Similar behaviour is seen in the profiles of l_z^+ for Bi10 and Bi20, reasons for which are not clear. Except very close to the wall, the azimuthal integral length scale $l_{r\theta}^+$ increases with increasing τ_y which indicates wider turbulent streaks for higher τ_y . For a given τ_y , $l_{r\theta}^+$ increases up to a certain y^+ and then decreases with further increasing y^+ . This is because there is only a finite space available for a turbulent eddy to grow in the azimuthal direction for a given r which decreases to zero at the pipe centre.

3.1.1. Mean axial velocity and viscosity

Profiles of the mean axial velocity U_z^+ are shown in Fig. 6(a) and compared to the Newtonian profile. For ease of discussion the flow region is divided into four regions, the viscous sublayer ($y^+ < 5$), buffer layer ($5 < y^+ < 30$), log layer ($30 < y^+ < 200$) and the core region ($y^+ > 200$). Although this kind of classification is common for

Newtonian fluids [20], bounds of the flow regions are not obvious for non-Newtonian fluids. The mean axial velocity profiles show yield-stress-dependence only outside the viscous sublayer and in the viscous sublayer, the effect of τ_y is negligible. The mean axial velocity U_z^+ is larger for higher τ_y for $y^+ \gtrsim 15$, which corresponds to a higher flow rate. In the log layer, U_z^+ profiles for all τ_y show a log region, however, they shift above the Newtonian profile with increasing τ_y . The effect of τ_y on the mean velocity gradient is marginal (Fig. 6 b) and it appears primarily over the range of $y^+ \in [8 - 80]$. These results are in contrast to those of shear thinning alone in PL fluids in which U_z^+ increases at all y^+ and the mean axial velocity gradient increases noticeably in the log layer (Figs. 8 and 11 in [18]).

Increasing τ_y affects the mean viscosity ν^+ in a similar way to shear thinning. For a given τ_y , the mean viscosity ν^+ is almost uniform in the viscous sublayer, but increases rapidly with y^+ beyond $y^+ \approx 10$ (Fig. 7). Similar to the mean axial velocity, ν^+ also shows yield-stress-dependence mainly outside the viscous sublayer where it is larger for higher τ_y . For Bi20, it is almost fifteen times larger than the nominal wall viscosity ν_w at the pipe centre. This is expected because the shear rate $\dot{\gamma}$ decreases with y^+ and the viscosity of a Bingham fluid increases with increasing τ_y when $\dot{\gamma} < \dot{\gamma}_w$ (see Fig. 2 a). Unlike PL fluids, the mean viscosity profiles of Bingham fluids do not show a clear log region (see Fig. 9 in [18]).

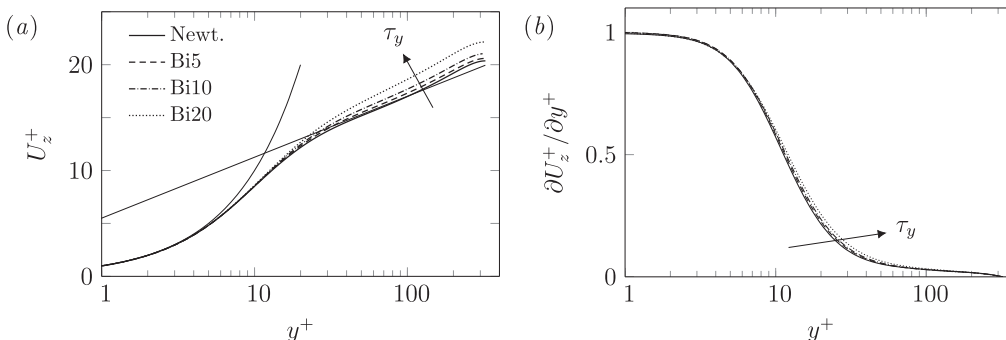


Fig. 6. Profiles of the (a) mean axial velocity and (b) its gradient plotted for different τ_y . The mean axial velocity increases with τ_y , whereas its gradient is only marginally affected by increasing τ_y , mostly in the buffer layer.

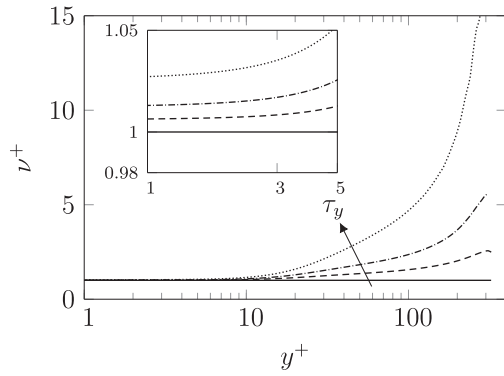


Fig. 7. Profiles of the mean viscosity plotted for different τ_y . The inset figure shows a closer look of the mean viscosity profiles in the viscous sub-layer. Arrow shows the sense of increasing τ_y . For the line legend see Fig. 6. Mean viscosity increases with increasing τ_y for all y^+ but the effect is seen mainly outside the viscous sublayer.

3.1.2. Mean shear stress budget

For a pipe flow of an incompressible fluid, the mean axial momentum equation is written as:

$$-\frac{1}{\rho} \frac{\partial P}{\partial z} + \frac{1}{r} \frac{\partial (r \bar{\tau}_{rz})}{\partial r} = 0 \quad (8)$$

Here, $\bar{\tau}_{rz}$ is the (r, z) component of the total mean shear stress tensor given as:

$$\bar{\tau}_{rz} = \bar{\nu} \frac{\partial U_z}{\partial y} - \overline{v'_r v'_z} + 2 \overline{v'_s s'_r} \quad (9)$$

$$= \tau_{rz}^v + \tau_{rz}^R + \tau_{rz}^{fv} \quad (10)$$

where τ^v is the mean viscous stress, τ^R is the Reynolds stress and τ^{fv} is the turbulent viscous stress which is non-zero only for non-Newtonian fluids. In the time averaged flow, only the (r, z) component of mean shear stress tensor survives, therefore, the subscript rz is omitted in the following discussion for clarity. Integrating Eq. (8) leads to

$$\bar{\tau} = \frac{r}{2} \frac{\partial P}{\partial z} \quad (11)$$

which can be expressed in wall units as:

$$\tau^+ = 1 - \frac{y^+}{Re_\tau} \quad (12)$$

Eq. (12) shows that for a given Re_τ , the mean shear stress τ^+ is independent of the fluid rheology and therefore, any change in one shear stress component must be balanced by changes in others.

Profiles of the mean shear stress components are plotted for different τ_y in Fig. 8(a) and (b) on linear y^+ axis and log y^+ axis. For a given τ_y , the mean viscous stress $\tau^{v+} = \nu^+ \partial U_z^+ / \partial y^+$ decreases monotonically with y^+ . For a given y^+ , τ^{v+} is larger for higher τ_y (Fig. 8). The latter is mainly due to higher mean viscosity ν^+ for higher τ_y as we have seen that $\partial U_z^+ / \partial y^+$ is only slightly affected by τ_y (see Fig. 6 b). Note that τ^{v+} at the wall is by definition is a comparison of the mean wall shear stress calculated using the mean velocity gradient and the mean pressure drop. It can be seen that τ^{v+} is slightly higher than one for $\tau_y > 0$, which suggests the mean wall shear stress calculated from the mean velocity gradient will slightly be in error. The increase in τ^{v+} with τ_y is mostly compensated for by a decrease in Reynolds shear stress τ^{R+} . Similar to a shear-thinning fluid (Fig. 10 in [18]), the turbulent viscous stress τ^{fv+} is negative for all τ_y . It increases in magnitude with increasing τ_y and decreases with y^+ vanishing at the pipe centre. The turbulent viscous stress only marginally (less than 5%) contributes in the total mean shear stress budget. Overall, these results are similar to those of shear-thinning PL fluids except for the behaviour of the turbulent viscous stress τ^{fv+} . It is less near the wall and larger near the centre which is opposite to that

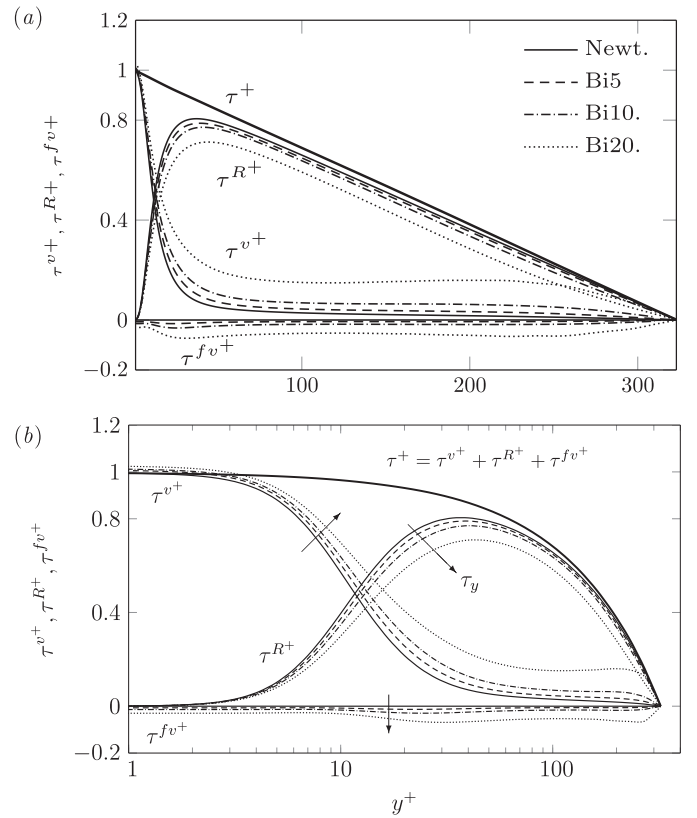


Fig. 8. Profiles of the mean viscous stress τ^{v+} , Reynolds shear stress τ^{R+} and the turbulent viscous stress τ^{fv+} plotted for different τ_y on (a) linear y^+ axis and (b) log y^+ axis. The thick line shows the profiles of the total mean shear stress which is the same for all cases and plotted here only for the Newtonian fluid. Increasing τ_y increases τ^{v+} and τ^{fv+} (in magnitude) but decreases τ^{R+} .

seen for pure shear-thinning fluids (see Fig. 10 in [18]).

3.1.3. Turbulence intensities

Profiles of the turbulence intensities show that the axial turbulent intensity, $u_z'^+$, is higher for higher τ_y and the peak shifts slightly away from the wall (Fig. 9). In contrast, the radial and azimuthal turbulence intensities ($u_r'^+$ and $u_\theta'^+$) are lower for higher τ_y . This is similar to the effect of shear thinning in PL fluids (Fig. 15 in [18]). The net effect of changes to turbulence intensities with τ_y is seen in the turbulent kinetic energy (k^+) profiles (Fig. 9 b). The turbulent kinetic energy k^+ increases with τ_y for $y^+ \lesssim 80$. This increase is a result of increasing $u_z'^+$ with τ_y which dominates the decrease in $u_r'^+$ and $u_\theta'^+$. However, the trend reverses for $y^+ \gtrsim 100$ and k^+ decreases with increasing τ_y . This is because the effect of τ_y on $u_z'^+$ diminishes there whereas contribution for $u_r'^+$ and $u_\theta'^+$ continues to decrease with τ_y . A noticeable difference in k^+ profiles compared to PL fluids is that the k^+ profiles for different n collapse in the core (Fig. 23 in [18]) but the profiles for different τ_y do not. The reason and the consequence of this is not clear. It is hypothesised that this is due to the significantly increased viscosity in the core which is generally higher for Bingham than PL fluids.

3.1.4. Turbulent kinetic energy budget

For a non-Newtonian fluid, an equation for the ensemble-average turbulent kinetic energy (TKE, $k = \frac{1}{2} \overline{u_i' u_i'}$) is written as [15]:

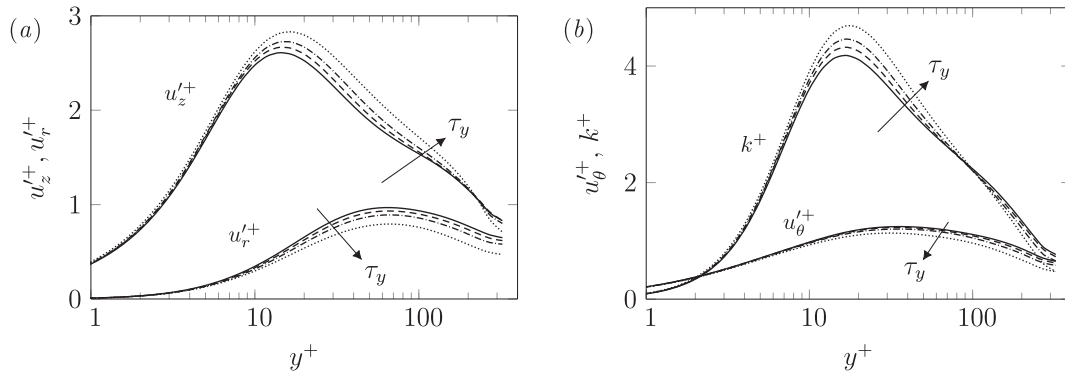


Fig. 9. Profiles of turbulence intensities (a) in the axial and the radial directions (b) in the azimuthal direction and turbulent kinetic energy plotted in wall coordinates for different τ_y . Arrow shows the sense of increasing τ_y . For the line legend see Fig. 8. Turbulence intensity increases in the axial direction but decreases in the radial and the azimuthal direction with increasing τ_y .

$$\begin{aligned} \frac{k_t}{\partial t} + U_j \frac{\partial k}{\partial x_j} &= \underbrace{\mathcal{P}}_{-u_i' u_j' S_{ij}} + \left\{ \underbrace{\mathcal{F}}_{\frac{1}{2} \frac{\partial u_i' u_j' u_i'}{\partial x_j}} - \underbrace{\Pi}_{\frac{\partial p' u_j'}{\partial x_j}} + \underbrace{\mathcal{D}}_{\frac{\partial (2\nu' s_{ij}' u_i')}{\partial x_j}} \right\} \underbrace{\epsilon}_{-2\nu' s_{ij}' s_{ij}'} \\ &+ \left\{ \underbrace{\xi_{nn}^+}_{\frac{\partial (2\nu' u_i' S_{ij})}{\partial x_j}} + \underbrace{\mathcal{D}_{nn}^+}_{\frac{\partial (2\nu' s_{ij}' u_i')}{\partial x_j}} \right\} \underbrace{\chi_{nn}^+}_{-2\nu' s_{ij}' S_{ij}} \underbrace{\epsilon_{nn}^+}_{-2\nu' s_{ij}' s_{ij}'} \end{aligned} \quad (13)$$

Here, the terms in the first row are non-zero for both Newtonian and non-Newtonian fluids. We refer these terms as Newtonian terms for which the following is a standard terminology:

- k_t : rate of change of turbulence kinetic energy;
- \mathcal{A} : mean flow advection;
- \mathcal{P} : turbulent kinetic energy production;
- \mathcal{F} : turbulent transport;
- Π : pressure-gradient work;
- \mathcal{D} : mean viscous transport;
- ϵ : mean viscous dissipation.

The terms in the second row are non-zero only for non-Newtonian fluids and we use the following terminology for these terms:

- ξ_{nn}^+ : mean shear turbulent viscous transport;
- \mathcal{D}_{nn}^+ : turbulent viscous transport;
- χ_{nn}^+ : mean shear turbulent viscous dissipation;
- ϵ_{nn}^+ : turbulent viscous dissipation.

The first two terms in Eq. (13), k_t and \mathcal{A} , vanish for a pipe flow which is temporally stationary and homogeneous. Turbulence receives energy from the mean flow via the turbulent kinetic energy production \mathcal{P} , which is dissipated via the turbulent dissipation term ϵ . The transport terms, Π , \mathcal{F} and \mathcal{D} , only redistribute TKE within the domain. Detailed explanation of these Newtonian TKE budget terms is available in [20–22].

In the non-Newtonian terms, the mean shear turbulent viscous transport, ξ_{nn}^+ , and the turbulent viscous transport, \mathcal{D}_{nn}^+ , are transport terms and therefore, either reinforce or oppose the transport by the Newtonian terms. The last two terms in Eq. (13) are the mean shear turbulent viscous dissipation, χ_{nn}^+ , and the turbulent viscous dissipation, ϵ_{nn}^+ , which increase or decrease the turbulent dissipation due to the Newtonian dissipation term ϵ .

Profiles of the TKE budget terms are plotted for different τ_y in Fig. 10, which are mostly qualitatively similar to those of shear-thinning PL fluids (Fig. 21 in [18]). TKE production, \mathcal{P}^+ , is lower for higher

τ_y (Fig. 10 a). Since $\mathcal{P}^+ = \tau^{R^+}(\partial U_z^+/\partial y^+)$ and $\partial U_z^+/\partial y^+$ is almost independent of τ_y (Fig. 6 b), lower \mathcal{P}^+ is mainly due to lower τ^{R^+} for higher τ_y (Fig. 8). In the y^+ range where \mathcal{P}^+ shows the strongest yield-stress-dependence, the mean viscous dissipation ϵ^+ is independent of τ_y . A similar trend was observed for shear-thinning PL fluids (Fig. 21 in [18]). At all other y^+ , the mean viscous dissipation ϵ^+ is larger (in magnitude) for higher τ_y . Increasing τ_y has the greatest effect on ϵ^+ outside the viscous sublayer which is in contrast to shear thinning (where ϵ^+ increases in magnitude in the viscous sublayer (Fig. 21 in [18])).

The total turbulent transport in the viscous sublayer is dominated by the mean viscous transport \mathcal{D}^+ which balances the mean viscous dissipation ϵ^+ there (Fig. 10 a). The mean viscous transport \mathcal{D}^+ is larger in magnitude for higher τ_y , however, the effect of τ_y is negligible outside the viscous sublayer. The remaining Newtonian transport terms, the turbulent transport, \mathcal{F}^+ , and the pressure-gradient work, Π^+ , show yield-stress-dependence only in the buffer layer ($y^+ \approx 7 - 30$, see Fig. 10 a and b). The pressure-gradient work Π^+ is small compared to other Newtonian transport terms and it decreases in magnitude with increasing τ_y whereas the effect of increasing τ_y is marginal on \mathcal{F}^+ .

The non-Newtonian terms which arise from viscosity fluctuations, are plotted in Fig. 10 (c)–(e). The non-Newtonian transport terms, ξ_{nn}^+ and \mathcal{D}_{nn}^+ , are significant only for $y^+ \lesssim 50$. Although they change sign with y^+ , they are larger in magnitude for higher τ_y at a given y^+ . The mean shear turbulent viscous transport ξ_{nn}^+ has a sign opposite to the mean viscous transport \mathcal{D}^+ over most y^+ and therefore, reduces the Newtonian transport terms (Fig. 10 c). The turbulent viscous transport, \mathcal{D}_{nn}^+ , is approximately three times smaller than ξ_{nn}^+ . The overall effect of the non-Newtonian transport terms is to decrease the magnitude of total transport with the effect being larger for higher τ_y (Fig. 11). This is similar to the effect of shear thinning in PL fluids (Fig. 21 in [18]).

The yield-stress-dependence of the non-Newtonian dissipation terms is also similar to that of shear thinning alone. Both non-Newtonian dissipation terms, χ_{nn}^+ and ϵ_{nn}^+ , are positive for Bingham fluids (Fig. 10 e) and they are larger in magnitude for higher τ_y . The mean shear turbulent viscous dissipation χ_{nn}^+ is maximum near the wall and decreases with y^+ vanishing somewhere in the log-layer depending on the value of τ_y . The turbulent viscous dissipation ϵ_{nn}^+ is small in the viscous sublayer (about 1/3rd of χ_{nn}^+), it reaches a minimum at $y^+ \approx 10$ and then starts increasing with y^+ . The location where ϵ_{nn}^+ peaks shifts away from the wall with increasing τ_y .

In the viscous sublayer, the total dissipation, $\epsilon^{k^+} = \epsilon^+ + \chi_{nn}^+ + \epsilon_{nn}^+$, decreases with increasing τ_y , due to positive χ_{nn}^+ and ϵ_{nn}^+ (Fig. 10 f) and the reduced dissipation persists until the start of the log layer ($y^+ \approx 30$). The total TKE transport, $T^{k^+} = \mathcal{F}^+ + \Pi^+ + \mathcal{D}^+ + \xi_{nn}^+ + \mathcal{D}_{nn}^+ + \epsilon_{nn}^+$, also decreases (in magnitude) near the wall ($y^+ < 60$) with increasing τ_y except near the edge of the viscous sublayer ($y^+ = 5$) where the profiles for different τ_y cross each other. Overall, the effect of increasing τ_y is seen

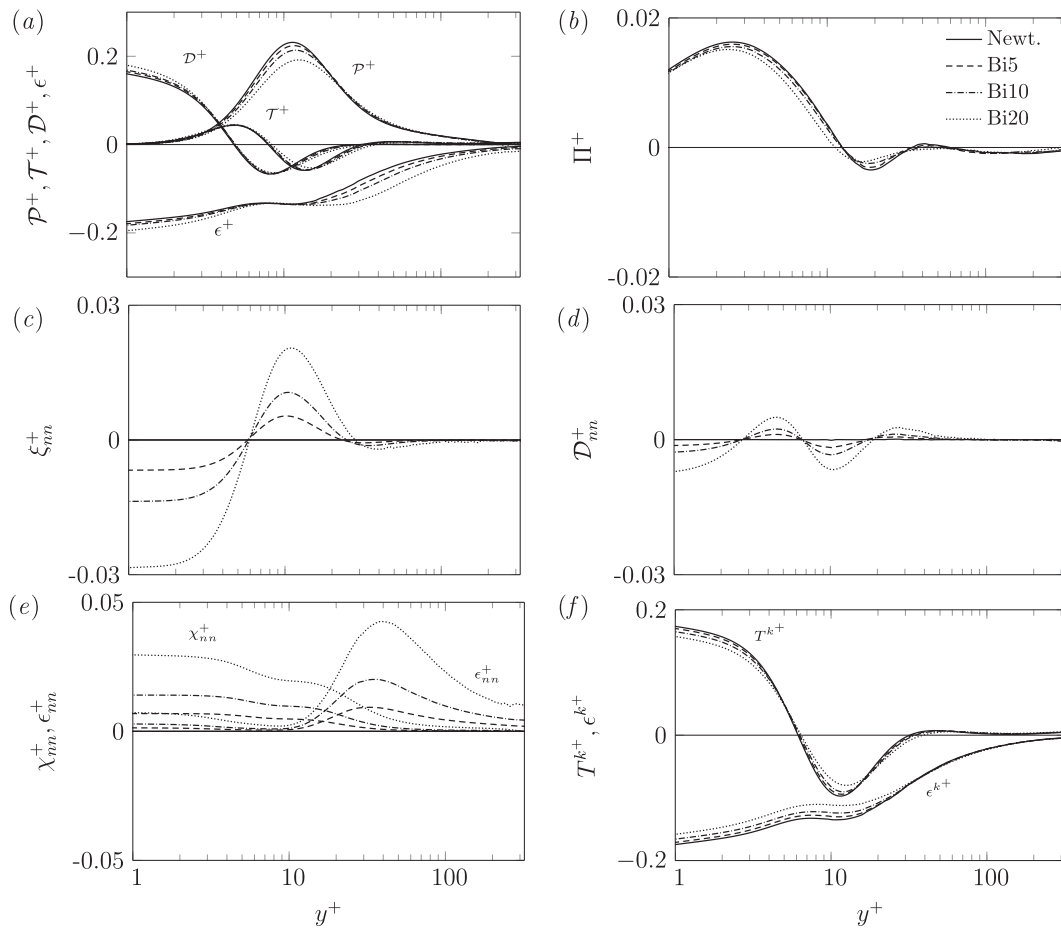


Fig. 10. Profiles of (a,b) Newtonian kinetic energy budget terms (c–e) non-Newtonian terms (f) sum of the Newtonian and non-Newtonian transport and dissipation terms plotted in wall units for different τ_y .

to have a notable effect on the TKE budget for $y^+ \lesssim 60$ which was also seen for PL fluids (Fig. 21 in [18]).

3.1.5. Summary

Results from Bingham fluids show that the effect of τ_y is greatest outside the viscous sublayer and seen more noticeably in the viscosity dependent terms, $\tau^{b+}, \epsilon^+, \chi_{nn}^+$ and ϵ_{nn}^+ . The mean axial velocity is also independent of τ_y in the viscous sublayer. This is in contrast to shear thinning which showed the greatest effect inside the viscous sublayer [18].

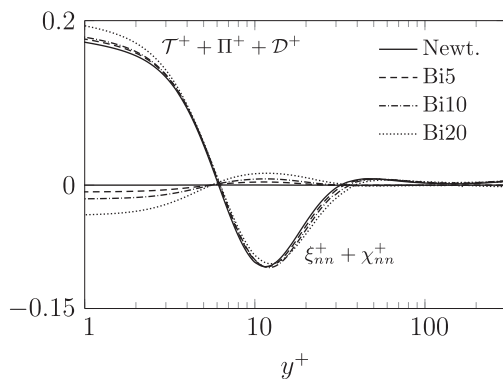


Fig. 11. Profiles of the sum of the Newtonian and non-Newtonian transport terms. The non-Newtonian transport usually opposed the Newtonian transport.

3.2. Modification of the yield stress effect by shear thinning

Many fluids in applications show both yield stress and shear-thinning behaviour and can be modelled with the HB rheology model. In order to see the joint effect of shear thinning and τ_y , the results of a shear-thinning PL fluid with $n = 0.8$ (referred to as PL) and the Bingham fluid, Bi10, are compared with those of a HB fluid with the same flow index as the shear-thinning fluid ($n = 0.8$) and τ_y as the Bingham fluid ($\tau_y^+ = 0.10$) at $Re_\tau = 323$. The HB fluid is referred to as HB10 in the following discussion.

The fluid viscosity for the three fluids PL, Bi10 and HB10 is plotted in Fig. 2 (b). Since ν_w is fixed, the viscosity profiles for PL, HB and Bi10 cross each other at the wall shear rate, $\dot{\gamma}^+ = 1$. Except in a range $\dot{\gamma}^+ \in [0.2, 1]$, the PL viscosity is lower than Bi10. In contrast, HB10 consistently shows higher viscosities than Bi10 for $\dot{\gamma}^+ < 1$ and lower for $\dot{\gamma}^+ > 1$. Contours of the instantaneous axial velocity near the wall show qualitatively similar flow for PL and Bi10 (Fig. 12). As expected, less disordered motion and low speed streaks running longer are seen in HB10 compared to other cases, which suggests that the flow of HB10 is closer to transition than the other cases. Since the instantaneous flows for PL and Bi10 are qualitatively very similar, the results of these two fluids are compared first before considering the joint effect of τ_y and shear thinning in HB10.

3.2.1. Comparison of power-law and Bingham rheologies

The mean axial velocity (U_z^+) profiles of PL and Bi10 almost overlap at all y^+ (Fig. 13 a), however, a close look via the mean axial velocity gradient $\partial U_z^+ / \partial y^+$ shows that U_z^+ is slightly higher (approximately 2%)

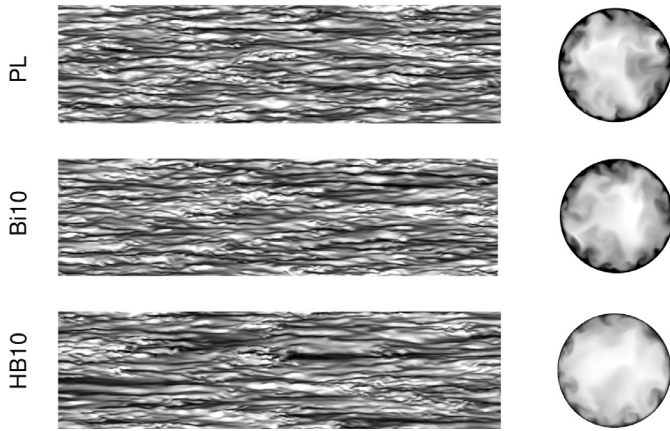


Fig. 12. Instantaneous axial velocity contours (left) at $y^+ = 10$ shown on developed cylindrical surfaces and (right) at a cross section in the middle of the domain plotted for (from top) HB fluids and Bi10. Flow is from left to right, and lighter grey represents higher speed. Flow becomes more transitional as the yield stress is increased or the fluid becomes more shear-thinning.

for the PL fluid than Bi10 in the viscous sublayer (Fig. 13 b). Outside the viscous sublayer, the profiles of $\partial U_z^+ / \partial y^+$ for PL and Bi10 overlap (marker and solid line). In contrast, profiles of the mean viscosity ν^+ overlap for PL and Bi10 only very near the wall (Fig. 14 a). Away from the wall, Bi10 clearly shows significantly higher mean viscosity than PL, which is expected from their viscosity plots (Fig. 2). Shear rate decreases with y^+ and for low shear rates Bi10 shows higher viscosity than PL.

Similar to the mean axial velocity, profiles of the axial turbulence intensity $u_z'^+$ and Reynolds shear stress τ^{R^+} also overlap for PL and Bi10 (Fig. 14 b) whereas profiles of radial and azimuthal turbulence intensities ($u_r'^+$ and $u_\theta'^+$) deviate from each other outside the viscous sublayer (Fig. 14 c). The turbulent viscous stress τ^{ν^+} is slightly lower (in magnitude) for Bi10 than PL in the viscous sublayer and the trend reverses for $y^+ > 10$ (Fig. 14 d). Since the Reynolds shear stress profiles overlap for these two cases (Fig. 14 b) and the total mean shear stress is independent of rheology (see Section 3.1.2), the reduced τ^{ν^+} in the viscous sublayer in Bi10 is balanced by a corresponding decrease in the mean viscous stress τ^{v^+} as seen in Fig. 14 (d). In the TKE budget, the viscosity dependent terms, $\mathcal{D}^+, \epsilon_{nm}^+, \xi_{nm}^+, \mathcal{D}_{nm}^+, \chi_{nm}^+$ and ϵ_{nm}^+ , are larger in magnitude for PL than Bi10 near the wall ($y^+ \lesssim 15$) but, the trend changes away from the wall (Fig. 15).

Overall the results of PL and Bi10 are mostly similar qualitatively and quantitatively except for a few differences seen for the mean viscosity and the non-Newtonian TKE budget terms.

3.3. Joint effect of shear thinning and the yield stress

HB10 includes both yield stress and shear thinning behaviour, therefore, as expected the mean axial velocity profiles of HB10 deviate

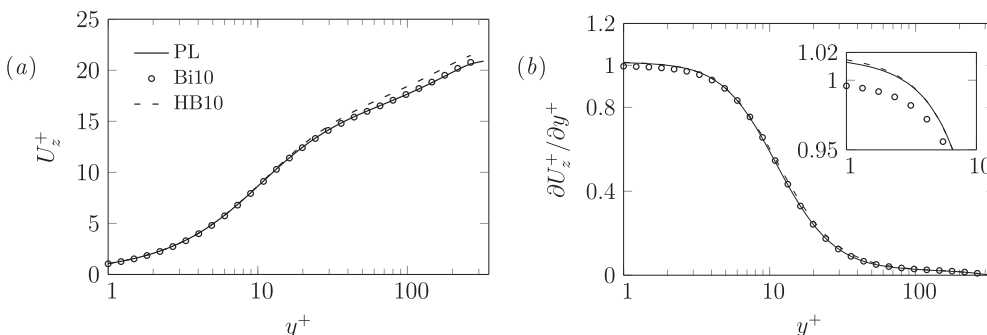


Fig. 13. Profiles of the (a) mean axial velocity, U_z^+ (b) and the mean axial velocity gradient, $\partial U_z^+ / \partial y^+$ plotted for PL, Bi10 and HB10.

above both PL and Bi10 (Fig. 13 a). In the viscous sublayer, profiles of the mean axial velocity gradient of HB10 and PL overlap (Fig. 13 b), which supports our argument presented for Bingham fluids in Section 3.1 that yield stress does not have a significant effect on the mean axial velocity in the viscous sublayer.

Since the mean viscosity ν^+ in the viscous sublayer is negligibly affected by increasing τ_y or shear thinning (Fig. 14 a and Fig. 9 in [18]), ν^+ profiles of HB10 overlap PL and Bi10 in the viscous sublayer. Outside the viscous sublayer, ν^+ profiles of HB10 deviate above the others (Fig. 14 a), which again shows that the yield stress has a prominent effect on ν^+ away from the wall.

The joint effect of shear thinning and τ_y is to increase the anisotropy of turbulent fluctuations, with increased $u_z'^+$ and decreased $u_r'^+$ and $u_\theta'^+$ outside the viscous sublayer (Fig. 14 b,c). Larger values of the turbulent viscous stress τ^{ν^+} are also seen for HB10 compared to other cases due to both shear thinning in the viscous sublayer and higher τ_y for $y^+ \gtrsim 10$ (Fig. 14 d). The larger values of τ^{ν^+} for HB10 lead to a higher mean viscous stress τ^{v^+} at the wall compared to other cases.

In the TKE budget, profiles of the transport terms and the TKE production for HB10 deviate from others only near the wall for $y^+ \lesssim 60$ (Fig. 15). As expected, the TKE production \mathcal{P}^+ is minimum for HB10 for a given y^+ due to the joint effect of shear thinning and τ_y . In contrast, the mean viscous transport \mathcal{S}^+ and the mean viscous dissipation ϵ^+ are maximum for HB10 (Fig. 15 a). The mean viscous dissipation (ϵ^+) profile of HB10 closely follows the profile of PL in the viscous sublayer and the profiles of Bi10 outside the viscous sublayer. Profiles of the non-Newtonian terms for HB10 closely follow the profiles of their sum for PL and Bi10 (Fig. 15 b–d). These are more influenced by shear thinning in the viscous sublayer and by τ_y outside it.

In summary, the combined effect of shear thinning and yield stress is that all deviations observed for τ_y are increased in effect. The effects are additive but not linear. Shear thinning in the HB rheology modifies the flow primarily in the near wall region.

4. Summary and conclusions

The current study investigates the effect of yield stress τ_y on turbulent pipe flow of a GN fluid using DNS. The friction Reynolds number is fixed at 323. Results show that the effect of increasing τ_y is mostly similar to shear thinning as reported in [18]. The axial velocity fluctuations are correlated for a larger distance for higher τ_y . The bulk velocity increases giving a lower friction factor with increasing τ_y . Mean fluid viscosity increases significantly outside the viscous sublayer with increasing τ_y . Increasing the yield stress increases the turbulence anisotropy by increasing the axial turbulence intensity but decreasing the radial and azimuthal turbulence intensities. Yield stress gives negative turbulent viscous stress which increases in magnitude with further increasing τ_y . Due to the non-zero turbulent viscous stress at the wall, the mean wall shear stress calculated from the mean velocity gradient will be slightly in error for the fluids considered here. The mean viscous stress is also higher for higher τ_y but the Reynolds shear stress decreases

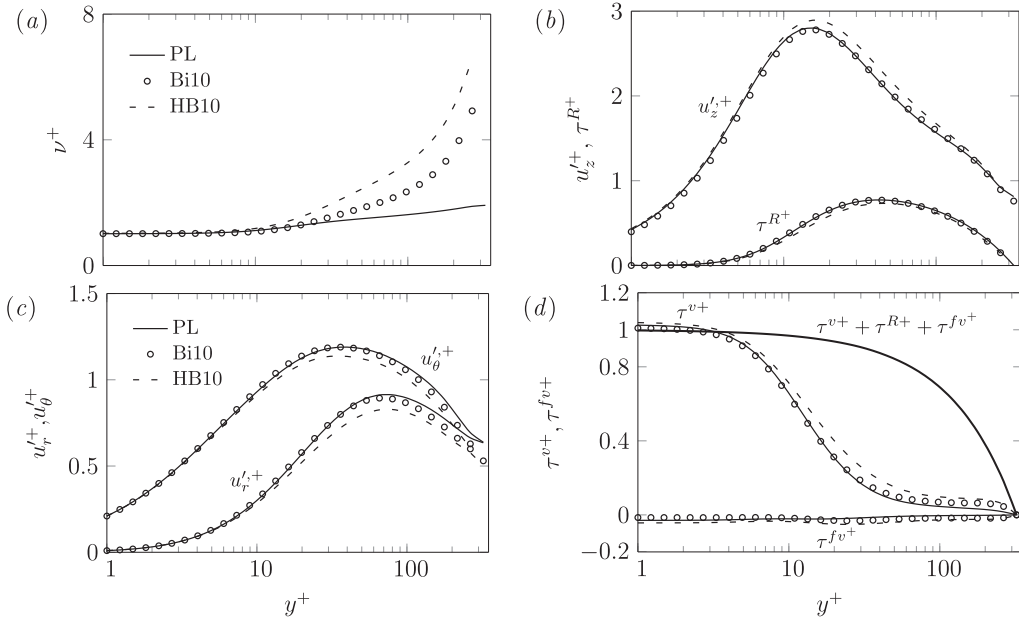


Fig. 14. Profiles of (a) axial and radial turbulence intensities (b) azimuthal turbulence intensities (c) mean viscosity and (d) the mean viscous stress τ^{v+} and the turbulence viscous stress τ^{fv+} plotted for HB fluids (lines) and Bi10 (markers).

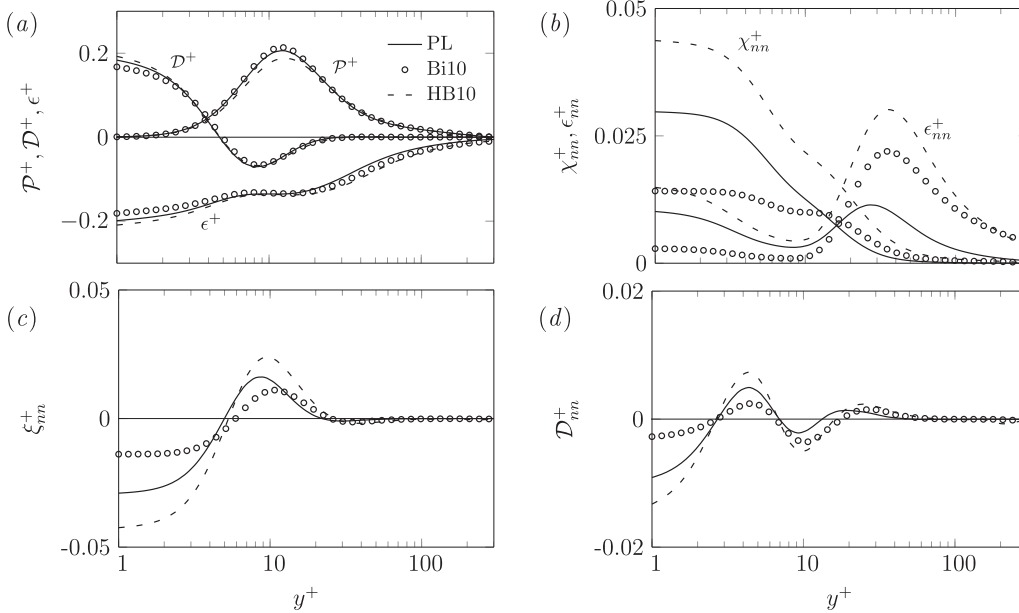


Fig. 15. Profiles of turbulence kinetic energy budget terms plotted in wall units for PL (solid line), Bi10 (markers) and HB10 (dashed line).

outside the viscous sublayer with increasing τ_y .

The effect of increasing τ_y on the turbulent kinetic energy budget is also similar to that of shear thinning. The turbulent kinetic energy budget terms show yield-stress-dependence mostly near the wall for $y^+ \lesssim 60$. Increasing τ_y decreases the turbulent kinetic energy production but increases the mean viscous dissipation. However, the new dissipation terms introduced due to viscosity fluctuations decrease the total turbulent kinetic energy dissipation. The combined effect of shear thinning and the yield stress is that all deviations observed for τ_y alone are increased in effect. The effects are additive but not linear.

Although the effect of increasing τ_y is similar to shear thinning, there are a few key differences. The effect of τ_y is minimum in the viscous sublayer and is larger outside the viscous sublayer as seen in the profiles of the turbulent viscous stress and the viscosity dependent terms in the turbulent kinetic energy budget. This is in contrast to shear thinning which affected flow the most inside the viscous sublayer. Because the turbulent viscous stress is almost zero for a Bingham fluid

in the viscous sublayer, varying τ_y does not affect the mean axial velocity inside the viscous sublayer to any notable extent. This is again in contrast to shear thinning which increases the mean axial velocity inside the viscous sublayer [18].

The current study suggests that the effect of yield stress on turbulence is confined near the wall for $y^+ \lesssim 60$. However, it is not clear that how this yield-stress-dependent region will be affected at higher Reynolds number. Further investigations are also required to confirm whether the effect of yield stress will persist at higher Reynolds number or it will vanish and the results of Bingham fluids will collapse on the Newtonian results.

Acknowledgements

The first author was supported by an industrial project AMIRA-P1087 funded through AMIRA International. Computations were carried out using the resources provided by the Pawsey Supercomputing

Centre with funding from the Australian Government and the Government of Western Australia via the NCI merit allocation scheme grant number D77. We gratefully acknowledge the resources and their support.

References

- [1] D.J. Hallbom, Pipe Flow of Homogeneous Slurry, Ph.D. thesis, Citeseer, 2008.
- [2] R. Chhabra, J. Richardson, Non-Newtonian Flow and Applied Rheology (second edition), Elsevier, 2008.
- [3] A.A. Townsend, The Structure of Turbulent Shear Flow, Cambridge University Press, 1980.
- [4] R. de Kretser, P.J. Scales, D.V. Boger, Improving clay-based tailings disposal: case study on coal tailings, *AIChE J.* 43 (7) (1997) 1894–1903.
- [5] J.T. Park, R.J. Mannheimer, T.A. Grimley, T.B. Morrow, Pipe flow measurements of a transparent non-newtonian slurry, *ASME J. Fluid Eng.* 111 (1989) 331–336.
- [6] J. Peixinho, C. Nouar, C. Desaubry, B. Théron, Laminar transitional and turbulent flow of yield stress fluid in a pipe, *J. Nonnewton. Fluid Mech.* 128 (2) (2005) 172–184.
- [7] M. Rudman, H.M. Blackburn, L.J.W. Graham, L. Pullum, Turbulent pipe flow of non-newtonian fluids, *J. Non-Newton. Fluid Mech.* 118 (1) (2004) 33–48.
- [8] M. Rudman, H.M. Blackburn, Direct numerical simulation of turbulent non-newtonian flow using a spectral element method, *Appl. Math. Model.* 30 (2006) 1229–1248.
- [9] M.R. Malin, Turbulent pipe flow of Herschel–Bulkley fluids, *Int. Commun. Heat Mass Transf.* 25 (3) (1998) 321–330.
- [10] J. Peixinho, C. Nouar, C. Desaubry, B. Théron, Laminar transitional and turbulent flow drag reduction asymptote, *J. Non-Newton. Fluid Mech.* 128 (2005) 172–184.
- [11] A.B. Metzner, J.C. Reed, Flow of non-newtonian fluids – correlations for laminar, transition and turbulent flow regimes, *A.I.Ch.E. J.* 1 (1955) 434–444.
- [12] F.T. Pinho, J.H. Whitelaw, Flow of non-newtonian fluids in a pipe, *J. Non-Newton. Fluid Mech.* 34 (2) (1990) 129–144.
- [13] G.P. Roberts, H.A. Barnes, New measurements of the flow-curves for carbopol dispersions without slip artefacts, *Rheol. Acta* 40 (5) (2001) 499–503.
- [14] J. Singh, M. Rudman, H.M. Blackburn, A. Chryss, L. Pullum, L.J.W. Graham, The importance of rheology characterization in predicting turbulent pipe flow of generalized newtonian fluids, *J. Non-Newton. Fluid Mech.* 232 (2016) 11–21.
- [15] F.T. Pinho, A GNF framework for turbulent flow models of drag-reducing fluids and a proposal for a $k-\epsilon$ type closure, *J. Non-Newton. Fluid Mech.* 114 (2003) 149–184.
- [16] M.R. Malin, Turbulent pipe flow of power-law fluids, *Int. Commun. Heat Mass Transf.* 24 (1997) 977–988.
- [17] D.O.A. Cruz, F.T. Pinho, Turbulent pipe flow predictions with a low Reynolds number $k-\epsilon$ model for drag-reducing fluids, *J. Non-Newton. Fluid Mech.* 114 (2003) 109–148.
- [18] J. Singh, M. Rudman, H.M. Blackburn, The influence of shear dependent rheology on turbulent pipe flow, *J. Fluid Mech.* 822 (2017) 848–879.
- [19] H.M. Blackburn, S.J. Sherwin, Formulation of a galerkin spectral element–fourier method for three-dimensional incompressible flows in cylindrical geometries, *J. Comput. Phys.* 197 (2) (2004) 759–778.
- [20] S.B. Pope, *Turbulent Flows*, Cambridge University Press, 2000.
- [21] P.A. Davidson, *Turbulence: An Introduction for Scientists and Engineers*, Oxford University Press, 2015.
- [22] J.G.M. Eggels, Direct and Large Eddy Simulation of Turbulent Flow in a Cylindrical Pipe Geometry, Ph.D. thesis, Delft University, 1994.